# Using Image Warping for Time-lapse Image Domain Wavefield Tomography

**Di Yang*, Alison Malcolm*, Michael Fehler***

* *Earth Resource Lab,*

*77 Mass Ave,*

*Cambridge, MA, 02139*

*Email: diyang@mit.edu; fehler@mit.edu; amalcolm@mit.edu.*

(March 12, 2014)

**GEO-2013-0424**

Running head: **Time-lapse Image Domain Wavefield Tomography**

## ABSTRACT

Time-lapse seismic data are widely used for monitoring subsurface changes. A quantitative assessment of how reservoir properties have changed allows for better interpretation of fluid substitution and fluid migration during processes like oil and gas production, and carbon sequestration. Full waveform inversion has been proposed as a way to retrieve quantitative estimates of subsurface properties through seismic waveform fitting. However, for some monitoring systems, the offset range versus depth of interest is not large enough to provide information about the low wavenumber component of the velocity model. In this study, we present an image domain wavefield tomography method (IDWT) using the local warping between baseline and monitor images as the cost function. This cost function is sensitive to volumetric velocity anomalies, and capable of handling large velocity changes with very limited acquisition apertures, where traditional full waveform inversion fails. In this paper,

we first describe the theory and workflow of our method. Layered model examples are used to investigate the performance of the algorithm, and its robustness to velocity errors and acquisition geometry perturbations. The Marmousi model is used to simulate a realistic situation in which IDWT successfully recovers time-lapse velocity changes.

# INTRODUCTION

Time-lapse seismic monitoring is often applied for reservoir management in the oil industry to obtain information about reservoir changes. It helps identify bypassed oil to be targeted for infill drilling, which extends the economic life of a field (Lumley, 2001). It is also capable of monitoring the progress of fluid fronts, providing information for injection optimization in enhanced oil recovery, and long-term fluid storage like carbon sequestration (Bickle et al., 2007). Generally, one baseline survey and subsequent monitoring surveys are acquired over time. Analysis and comparison of the datasets provides an estimate of changes in seismic velocity and mass density. These changes are related to changes in dynamic reservoir properties like pore pressure and fluid saturation (Dadashpour et al., 2008), which are important in reservoir simulation and interpretation.

For a time-lapse seismic dataset, information about the changes in model parameters in the target zone can be categorized into two groups: amplitude changes and time shifts. Amplitude changes could be induced by new scattering in the target interval, or differences in reflectivity at the interfaces. Time shifts are the response to a physically shifted geologic interface (e.g. a compacting reservoir), or a velocity perturbation along the signal's ray-path. To better link the changes in measured signals to inferred reservoir responses, it is essential to quantify the changes from different mechanisms. In some time-lapse seismic analysis, the time shift information is omitted because the monitor data or images are aligned with the baseline to compare the amplitudes. In other studies, time shifts picked at certain horizons are used to study the reservoir velocity changes, or the strain field changes above the reservoir (Barkved and Kristiansen, 2005; Landrø and Stammeijer, 2004). However these analyses are conducted on post-stack data, which have already lost some information

during the stacking process. In this study, we focus primarily on time shifts in pre-stack data, and velocities in model space. We do not consider amplitude changes, which can be better inverted or interpreted after the inversion for a corrected time-lapse velocity model.

To recover the seismic velocities, full waveform inversion (FWI) (Tarantola, 1984; Virieux and Operto, 2009) has been applied to individual surveys. The application of FWI to time-lapse data seems straight-forward, however, in practice it is constrained by the survey design, data quality and the nonlinear nature of FWI. Inversion strategies tailored for time-lapse data have addressed issues like repeatability, computation efficiency (Yang et al., 2012) and local minima (Watanabe et al., 2005; Denli and Huang, 2009; Yang et al., 2011; Asnaashari et al., 2011). Traditional FWI requires low-frequency data and large survey offsets to invert for the low-wavenumber component of the velocity model (Virieux and Operto, 2009). However, seismic surveys with large offsets are expensive particularly when the region of interest is relatively small. Small-offset reflection data do not provide constraints on the model from a wide enough range of different angles to allow for the estimation of low-wavenumber structures. With small offsets, FWI functions more like least-square migration which only finds reflectivity. Image-domain methods, often involving velocity analysis, have been proposed to obtain the low-wavenumber part of the velocity model from reflection data (Sun and Symes, 2012; Biondi and Almomin, 2012). Some image-domain methods are computationally expensive because they require the calculation of angle gathers or offset gathers, which require many sources and receivers. These methods are more suitable for initial model building. Shragge et al. (2013) extended an image-domain tomography method to 4D, however, the inverted velocity changes can be smeared.

When a seismic reflection is shifted in time, there is an ambiguity as to whether the reflector has shifted or there is a velocity change above the reflector. However, in many

cases, the changes in the depths of structures are not expected to be as significant as the depth shifts of the reflectors in images due to velocity changes. For example, the physical displacement of the reservoir boundaries caused by compaction may be only a fraction of a sampling interval of the migration image (e.g. half a meter per year in the North Sea (Barkved and Kristiansen, 2005)). However, volumetric strain in the overburden due to compaction may cause changes in its seismic velocities. Velocity in the reservoir itself might also change due to depletion or fluid substitution. In cases like $CO_2$ sequestration, large amounts of fluid are injected into the subsurface, without significant changes in pore pressure. Compared to physical structure changes, velocity changes are expected to be the dominant effect on time-lapse images from these settings (Arts et al., 2004). In this paper, we assume that seismic reflectors do not shift over the period during which time-lapse surveys are collected. We also assume that the waveforms reflected from interfaces in the targeted area do not change significantly. Based on this assumption, successive acquisitions that illuminate similar areas should produce similar images without depth shifts if correct velocity models are used.

In this paper, we present an image-domain wavefield tomography (IDWT) method specialized for time-lapse reservoir monitoring. With a baseline velocity model, migrated images for both baseline and monitor data can be produced with a reverse time migration algorithm. With the assumptions above, depth differences between images should be primarily caused by time-lapse changes in the velocity and not by physical changes in reflector position. Dynamic image warping (Hale, 2013) is used to measure the image shifts in a way that is robust to cycle skipping and amplitude differences between images. By minimizing the warping function (the shifts between baseline and monitor images), we invert for velocity changes iteratively using the adjoint-state method (Plessix, 2006). The inversion is

only sensitive to low-wavenumber velocity perturbations that control wavefield kinematics. The inverted velocity changes are found to be localized between reflectors, which aids interpretation of fluid migration like gas leakage. Yang et al. (2014) applied this method to time-lapse datasets from a $CO_2$ injection field. In this paper, we describe the theory and workflow of the IDWT approach. Synthetic examples are used to demonstrate its capability and limitations. The robustness of the method to baseline velocity errors and survey geometry non-repeatability is also investigated.

## THEORY

Iterative inversion methods like full waveform inversion, are designed to estimate model parameters by fitting observed data with simulated data. In the time-lapse IDWT method, the model parameters are seismic velocity changes, and the observed data are the migrated images that are constructed from baseline and monitor seismic surveys. We estimate velocity changes by matching monitor migrated images with baseline migrated images. The cost function here can be written as the L-2 norm of some measure of dissimilarity between two images. The simplest measure is the amplitude difference:

$$E_{subtract}(m) = \frac{1}{2} \sum_{x_s} \int_x \int_z |I_1(x, z, x_s) - I_0(x, z, x_s)|^2 dx dz, \tag{1}$$

where $I_0$ is the baseline image, $I_1$ is the monitor image, $x$ and $z$ are spatial coordinates, and $x_s$ is the source index. We derive all the equations here in 2D for simplicity, but the extension to 3D is straight-forward with one additional integral over the third spatial dimension. This cost function has the same drawback as the traditional FWI cost function. When reflector shifts are too large (> half wavelength, measured normal to the reflector), cycle skipping makes the cost function insensitive to local velocity perturbations. The direct

subtraction $I_1 - I_0$ also causes problems when the images have different amplitudes. These differences could be related to effects other than velocity perturbations. In these cases, even if the velocity model is correct, the cost function may not be minimized.

As described by Hale (2013), a migration image $I$ based on the incorrect velocity can be considered a warped version of the true image $\widetilde{I}$ based on the correct velocity. In Equation 2, $h(x,z)$ and $l(x,z)$ are warping functions that specify how much the image point at $(x,z)$ in $\widetilde{I}$ is shifted from the same image point in $I$ in horizontal (h) and vertical (l) directions.

$$I(x,z) = \widetilde{I}(x + h(x,z), z + l(x,z)). \tag{2}$$

Here we assume that the monitor image based on the baseline velocity model is a warped version of the baseline image. For images with reflection data, both vertical and lateral shifts can be measured (Cox and Hatchell, 2008; Hale et al., 2008). In this study, we only measure the vertical warping $l(x,z)$ for simplicity. The amount of vertical warping can be calculated by solving an optimization problem. Specifically we compute

$$w(x,z) = \arg\min_{l(x,z)} D(l(x,z)), \tag{3}$$

where

$$D(l(x,z)) = \int_x \int_z (I_1(x,z) - I_0(x, z + l(x,z)))^2 dxdz. \tag{4}$$

We use the dynamic warping algorithm (Hale, 2013) to solve the optimization problem above for the warping function $w(x,z)$.

Since the warping function decreases in magnitude as $I_1$ and $I_0$ become well aligned, we use the L-2 norm of $w(x,z)$ as the cost function:

$$E(m) = \frac{1}{2} \sum_{x_s} \int_x \int_z |w(x,z,x_s,m)|^2 dxdz, \tag{5}$$

where m is the squared slowness used for migrating monitor data, and $x_s$ is the source index. We invert for velocity $\frac{1}{\sqrt{m}}$ by minimizing $E(m)$ with a gradient-based method.

To calculate the gradient $G$, we use an adjoint-state method (Plessix, 2006). In full waveform inversion, the gradient is calculated by cross-correlating the forward propagated source wavefield and the back propagated residual wavefield (the adjoint wavefield). In IDWT, the gradient can be similarly written as a correlation between wavefields:

$$G(x,z) = -\sum_{x_s}\int_{t=0}^{T}(\frac{\partial^2\lambda_s(x,z,t,x_s)}{\partial t^2}u_s(x,z,t,x_s) + \frac{\partial^2\lambda_r(x,z,t,x_s)}{\partial t^2}u_r(x,z,t,x_s))dt, \quad (6)$$

where $u_s(x,z,t,x_s)$ and $u_r(x,z,t,x_s)$ are source and receiver fields from forward and backward propagation respectively. The associated adjoint wavefields are $\lambda_s(x,z,t,x_s)$ and $\lambda_r(x,z,t,x_s)$. The adjoint wavefields $\lambda$ are obtained by solving the wave equation:

$$m\frac{\partial^2\lambda(x,z,t)}{\partial t^2} - \Delta\lambda(x,z,t) = d, \quad (7)$$

where $m$ is the squared wave slowness, and $d$ is the adjoint source. The adjoint sources for solving for $\lambda_s(x,z,t,x_s)$ and $\lambda_r(x,z,t,x_s)$ are respectively:

$$d_s(x,z,t,x_s) = \alpha(x,z,x_s)u_r(x,z,t,x_s) \quad (8)$$

and

$$d_r(x,z,t,x_s) = \alpha(x,z,x_s)u_s(x,z,t,x_s), \quad (9)$$

in which

$$\alpha(x,z,x_s) = \frac{w(x,z,x_s)\frac{\partial I_0(x,z+w(x,z,x_s),x_s)}{\partial z}}{(\frac{\partial I_0(x,z+w(x,z,x_s),x_s)}{\partial z})^2 - \frac{\partial^2 I_0(x,z+w(x,z,x_s),x_s)}{\partial z^2}(I_1(x,z,x_s) - I_0(x,z+w(x,z,x_s),x_s))}. \quad (10)$$

The derivation is similar to the formula in differential semblance optimization (DSO) (Plessix, 2006). The details are presented in the appendix. The wavefield mask $\alpha(x,z,x_s)$

is oscillatory due to the term $\frac{\partial I_0(x,z+w(x,z,x_s),x_s)}{\partial x}$ in the numerator. The denominator in $\alpha(x,z,x_s)$ acts as an amplitude normalizer; in practice, we add a water-level term to the denominator to avoid dividing by zero. The warping function $w(x,z,x_s)$ tells us where $\alpha$ should be non-zero, and determines the sign of the adjoint source, which determines the sign of the velocity update. The implementation of the inversion process consists of the following steps:

Given a baseline velocity model $m_0$, and a baseline migration image $I_0$,

(i) for each shot $x_s$, migrate the monitor data with the velocity model $m_0$ used to produce $I_1(x,z,x_s)$

(ii) compute the vertical shifts $w(x,z,x_s)$ using dynamic warping

(iii) evaluate the cost function $E(m)$ after the summation over shots $x_s$, stop (if small enough) or go to the next step

(iv) for each shot $x_s$, compute the adjoint wavefields $\lambda_s$,$\lambda_r$, and the partial gradient $G(x,z,x_s)$

(v) sum $G(x,z,x_s)$ over all shots to form the gradient $G(x,z)$

(vi) update the velocity model with $G(x,z)$ to get $m_{i+1}$

(vii) remigrate the monitor data with the updated model $m_{i+1}$, and go to step (ii)

## EXAMPLES USING SYNTHETIC DATA

In this section, we will use synthetic data to show how the method works, and investigate its performance under different scenarios. First, a simple three-layer model is used to demonstrate IDWT's ability to recover low-wavenumber velocity changes. The performance

of IDWT with respect to number of shots is tested with the same model. A model with six layers is used to study the relation between IDWT resolution and the layer spacing. The robustness of IDWT to errors in the baseline velocity model is tested with two cases in which one large and one small Gaussian velocity errors are introduced. The robustness of IDWT to source-receiver geometry discrepancies between surveys is investigated for both correct and incorrect baseline velocity models. Finally, the Marmousi model is used to show how IDWT performs for a complicated velocity structure.

## Three-layer Model

The three-layer model has constant velocity ($v_p$=3000m/s) but different density in each layer (Figure 1(a)). A velocity anomaly is placed in the middle of the time-lapse model as shown in Figure 1(b). The shape of the anomaly is Gaussian with a maximum velocity increase of 800 m/s. We place 300 receivers (blue triangles in Figure 1(a)) at an interval of 10 meters, and 5 sources (red stars in Figure 1(a)) at an interval of 600 meters on the surface. The source is a Ricker wavelet with a center frequency of 25 Hz. We use a finite difference acoustic wave equation solver to generate the datasets. In this example, we assume the constant baseline velocity is known.

### *Imaging and Warping*

Reverse time migration (RTM) (Baysal et al., 1983; McMechan, 1983) is used to produce all the migration images during the inversion. The baseline and initial monitor images obtained using a single shot gather (the third shot in Figure 1(a)) are shown in Figure 1(c) and Figure 1(d), respectively. The position of the deeper reflector in the monitor image

(Fig 1(d)) is shifted vertically due to the velocity change in Figure 1(b). We compute $w(x, z)$ using the dynamic image warping algorithm (Hale, 2013) to describe how much $I_1$ is shifted from $I_0$, as shown in Figure 2. The maximum vertical shift is 4 grid points (40 meters). As in Equation 10, $w(x, z)$ is used to calculate a spatial weighting function $\alpha(x, z, x_s)$, to mask the wavefields $u_s$ and $u_r$ to form adjoint sources (Equations 8 and 9).

*Inversion Results Comparison*

Figure 3(a) shows the velocity model change recovered from IDWT with the five sources shown in Figure 1(a). The recovered anomaly is centered at the correct location, but it is smeared vertically due to the acquisition geometry. This vertical smearing is bounded by the two reflectors. If the inversion attempts to put any perturbation above the first reflector, the entire image will be shifted. IDWT will subsequently reduce this shift by reversing that perturbation. Some of the changes are positioned along the ray-paths due to limited source and receiver coverage. Within the area of the recovered anomaly, the amplitude is not correctly distributed, and the maximum velocity increase is only 50% of the true value.

Although the inverted velocity is not perfect, the monitor migrated image based on it (Fig 3(b)) shows reflectors at the same locations as in the baseline image (Fig 1(c)). The model from IDWT has the correct background kinematics, and is a good starting model for FWI. Figure 3(c) shows the velocity change determined with the application of a standard FWI (Tarantola, 1984) for the same monitor data using the velocity model obtained from IDWT as a starting model. Both the amplitude of the anomaly, and the distribution of the velocity are improved as FWI inverts more phase and amplitude changes.

For comparison, we compute a standard FWI on the monitor data starting from the correct baseline velocity and density models. Figure 3(d) shows the result. The inversion gives poor recovery of the velocity anomaly because of several issues. First, the velocity change is large enough to cause cycle skipping in the data domain. Second, FWI with this narrow-offset survey geometry reduces to least-squares migration, so that the volumetric velocity change is barely resolved. Instead, a reflector that does not exist in the true velocity model is generated to fit the data.

Figure 4 shows cost-function curves for IDWT, FWI, and FWI after IDWT. IDWT converges within 10 iterations, while FWI converges much slower, both after IDWT and for FWI alone. The cost function for FWI alone plateaus after 10 iterations, because the residual is insensitive to velocity perturbations, due to cycle-skipping. FWI after IDWT converges with a lower cost than does FWI alone, but remarkably slower than does IDWT. However IDWT requires four wavefield calculations to obtain the gradient in each iteration, and two wavefield calculations are required for one migration. Assuming each wave propagation calculation takes time $T$, and each line search takes 3 migrations, the actual computational cost of IDWT is 10 times that for computing $N$ wavefields, where N is the number of IDWT iterations. Similarly, because it requires 3 forward models per line search, one FWI iteration takes $5T$. In this example, to get the final model in Figure 3(c), we used 10 IDWT iterations, and 20 FWI iterations. Thus the total computation time is 200T, of which 50% is used in IDWT.

## Multi-layer Model

As shown in the three-layer model example, the smearing of the time-lapse velocity change is bounded by the reflectors. We expect that smaller reflector spacing will lead to a better determined anomaly. To investigate this, we use a multi-layer model to simulate the case where time-lapse changes span several layers. A constant velocity ($v_p$ = 3000 m/s) is used for the baseline model. The time-lapse velocity model is the same as that in Figure 1(b). A six-layer density model as shown in Figure 5(a) is used to generate reflections. Layer thicknesses in the center of the model are smaller than the size of the velocity anomaly in Figure 1(b).

Figure 5 shows the velocity changes resolved by IDWT using different numbers of shots. Only one single shot placed in the center on the surface is used in Figure 5(b). Compared with the results in Figure 3(a), the anomaly is much better constrained vertically by the second and fourth reflectors in the model. Correspondingly, the magnitude of the velocity anomaly is better recovered; 10 and 20 shots are used evenly spaced at intervals of 265 and 125 meters in Figure 5(c) and 5(d) respectively. The shape and relative magnitude distribution are improved with additional shots.

## Baseline Velocity Errors

For all the previous examples, we assumed that the baseline model was exactly known. In practice, it is more likely that the baseline velocity model we build is inaccurate. To study the robustness of IDWT to errors in the baseline velocity, we use the model in Figure 6(a), which contains a Gaussian-shaped low velocity zone, as the true baseline velocity model. We assume the anomaly is not resolved by the baseline velocity model building and so a

constant velocity model is used for the baseline migration. We use the density model in Figure 5(a) with 20 shots evenly spaced at an interval of 125 meters on the surface to generate synthetic data. The true time-lapse velocity model (Figure 6(c)) has an additional high velocity Gaussian-shaped anomaly, which is the net change between baseline and time-lapse models (Figure 6(b)). The peak magnitude of both anomalies is 200 m/s.

Figure 6(d) shows the IDWT result obtained when using 20 shots. Compared with the result obtained using the correct baseline model (Figure 5(d)), the resolved time-lapse anomaly maintains the same quality in both shape and magnitude. More importantly, there are no negative velocity changes apparent in the result. The baseline velocity model error (the negative Gaussian-shaped anomaly) is not carried over to the time-lapse inversion. In other words, IDWT detects only the relative changes in the models. A close scrutiny of Figure 5(d) and Figure 6(d) reveals that the shape of the resolved change is slightly distorted because of the kinematic error induced by the unknown Gaussian anomaly in Figure 6(a). We expect the distortion to get stronger with bigger errors in the baseline velocity model. We test this with the model shown in Figure 6(e), in which we increase the maximum amplitude of the low velocity error in the baseline model to 800 m/s. The IDWT result with 20 shots, shown in Figure 6(f), is severely distorted in shape but the amplitude and position are still accurately recovered.

### Source Geometry Non-repeatability

Seismic survey repeatability is a key factor in achieving successful time-lapse monitoring. One common issue is the discrepancy of source-receiver geometry between surveys. A small deviation of the source position in the monitor survey from that of the baseline, can lead to

large differences in waveforms, which makes direct comparison between datasets difficult. Time-lapse FWI methods, such as double-difference waveform tomography, which requires data subtraction (Denli and Huang, 2009; Watanabe et al., 2005), must carefully co-process the baseline and monitor datasets. In IDWT, instead of data, we compare images, which are less sensitive to shot position deviations. With the correct velocity model, neighboring sources should give very similar images. As a result, when they are migrated with the same baseline velocity, differences between a monitor image for shot position $x + \delta x$, and a baseline image for shot position $x$ should still relate to time-lapse velocity changes. We expect IDWT to be robust to this type of source geometry difference between surveys.

We employ the baseline velocity models used in previous examples, with the constant velocity, weak Gaussian anomaly (200 m/s), and strong Gaussian anomaly (800 m/s). The maximum value of the time-lapse change is 200 m/s. The density model is the same as that in Figure 5(a). For the baseline survey, 15 sources are evenly spaced at an interval of 170 meters, and 300 receivers are evenly spaced at an interval of 10 meters. For the monitor survey, we only consider source positioning errors. Because IDWT is conducted with shot gathers, the effects from receiver positioning errors should be negligible as long as they cover the same area. Two types of source positioning errors are commonly observed in practice: random perturbations (e.g. limited GPS precision), and systematic perturbations (e.g. feathering effects in acquisition).

For random perturbations, we randomly perturbed each source either one grid point left or one grid point right from its baseline position. The grid spacing is 10 meters in our tests, which is large compared to position errors observed in some well-repeated surveys in practice (Yang et al., 2013). In addition, position errors in reality would not be uniformly $\pm 10$ meters. However, we do not expect this to have a large effect on the results.

Figure 7 shows the IDWT results with different levels of baseline velocity errors but with the same randomly perturbed source positions. There is no baseline velocity error in Figure 7(a). The baseline velocity models used in Figure 7(b) and (c) have Gaussian-shaped errors of 200 m/s and 800 m/s peak value respectively. The one-to-one comparison between Figure 7(a), (b), (c) and Figure 5(d), Figure 6(d), Figure 6(f) show that the random source position perturbations have little effect on the performance of IDWT.

To study the effect of systematic perturbations, we move the monitor survey source positions uniformly towards the right. Three levels of shot position error are studied: $\delta x$ equals 10 meters, 20 meters and 50 meters. The monitor datasets are generated and migrated using the perturbed source locations. Figure 8(a), (b) and (c) show the IDWT results with the known constant baseline velocity model. The time-lapse velocity anomalies are resolved with the same quality in all three cases with increasing shot positioning error. Artifacts near the sources result from illumination differences between baseline and monitor surveys. As we discussed for the three-layer model, when the shot positions are the same in both surveys, the smeared updates near the sources are diminished by iteratively correcting the image of the shallower reflector. However, when the shot positions are different, as illustrated in Figure 9, parts of the monitor image have no corresponding parts in the baseline image (dashed circles). As a result, part of the velocity update cannot be constructed because the unconstrained parts of the image marked by arrows in Figure 9 are insensitive to that velocity change. At greater depth, this effect is mitigated by stacking shots, but the effect of stacking is weak near the sources. If the targeted area is deep in the subsurface, these artifacts will not affect the interpretation. If the monitor image is compared to the entire image formed by all the baseline shots, this effect will be eliminated because the shadowed areas in Figure 9 will be covered by baseline images of neighboring shots.

Figure 8(d), (e) and (f) show the IDWT results with a weak Gaussian velocity error (200 m/s) in the baseline model. As the shot positioning error increases, the error induced by the incorrect baseline velocity model, marked by black circles, gets stronger. The principle that neighboring shots should give similar images is violated because the baseline velocity is incorrect. As a result, differences between baseline and monitor images are caused by both the baseline velocity errors and the time-lapse velocity changes. The difference caused by baseline velocity error is bigger when two shots are further apart. Accordingly, velocity error increases as the shot positioning error increases. In addition, the velocity error is inverted with a reverse sign, because the monitor image is aligned with the incorrect baseline image. For example, if the low-velocity region in the baseline model is unknown (i.e., not included in the model for migration), the reflectors imaged by a source that illuminates the anomaly will be deeper than their true positions. Regardless of the time-lapse changes, IDWT would assume the baseline image is correct, and perturb the velocity to make monitor image reflectors deeper, leading to a high velocity update.

Figure 8(g), (h) and (i) show the IDWT results with the strong Gaussian velocity error (800 m/s) in the baseline model. As expected, the larger error induces bigger false changes (located inside the black circles) in the time-lapse inversions. In Figure 8(i), the false changes already have the same order of magnitude as the time-lapse changes when the source positioning error is 50 meters. In this case, an interpretation would likely be affected by the velocity error. However, an 800 m/s velocity error in the baseline model is significant, and source positioning errors of 50 meters are excessive in a well-repeated 4D seismic survey. Based on the tests shown in this section, we conclude that for relatively large errors in the baseline velocity model, and for both random and systematic source geometry discrepancies between surveys, IDWT is robust and expected to be capable of delivering useful inversion

results.

## Marmousi Model

For a more realistic synthetic test, we apply IDWT using the Marmousi model (Versteeg, 1994). As shown in Figure 10(a), only part of the original Marmousi model with complicated geologic structures is used to better simulate narrow-offset acquisition. Five shots evenly spaced at an interval of 200 meters (red stars) are used to generate the synthetic datasets, and 400 receivers are deployed on the surface at an interval of 5 meters. Figure 10(b) shows the true time-lapse velocity model with a velocity decrease in the layers at around 1900 meters depth. The actual boundary of the velocity anomaly is outlined by the black dashed line. The density is constant throughout the model.

We smooth the Marmousi model to generate the baseline model for migration as shown in Figure 11(a). Figure 11(b) shows the migrated image with one shot gather of the baseline datasets. Due to the limited aperture of the acquisition, some of the structures (marked by arrows in Figure 11(b)) are not illuminated. The layers in these areas are completely missing in the image. The reflectors above and below the layer containing the time-lapse changes (dashed line in Figure 11(b)) are clearly imaged.

The IDWT result obtained using these 5 shots is shown in Figure 12(b). The resolved anomaly is localized within the area enclosed by the dashed line. Both the shape and amplitude of the anomaly are well recovered. The true change, as shown in Figure 12(a), has small values near the boundary of the anomaly (dashed line). In contrast, the inverted change appears to be larger in size due to vertical smearing between reflectors. The arrow in Figure 12(b) points to a location where the inverted anomaly spreads beyond the boundary

of the actual anomaly but is well-constrained by the reflector below. The smearing occurs because the boundary of the true time-lapse change, marked by the arrow in Figurer 10(b), is in the middle of the layer. As we observed for the layered-model examples, velocity changes within a single interval are vertically smeared throughout the layer but bounded by the reflectors. With this limitation, IDWT is again effective in recovering the local time-lapse velocity change.

## DISCUSSION

From synthetic examples, we see that IDWT is able to robustly recover time-lapse velocity changes, with acquisition limitations, such as narrow offsets and survey non-repeatability. As with most tomography methods, IDWT smears velocity changes along wave-paths. However, the smearing effect is clearly bounded by reflectors above and below the changes. This effect is important for leakage monitoring when the ambiguity between the smearing and real leakage must be removed. Smaller differences between the boundary of the changes and the reflector boundaries lead to more reliable estimates of velocity changes. Better estimates of the velocity changes lead to more reliable interpretations of the changes.

In time-lapse inversions, we are interested in the relative changes between the surveys at different times. However, the data residuals due to the uncertainty in the baseline inversion are likely to contaminate the final result of time-lapse FWI. Tailored FWI schemes have been developed to suppress these sources of noise (Denli and Huang, 2009; Yang et al., 2011). In IDWT, errors in the baseline model affect both the baseline and monitor images. As the monitor images match the baseline ones, any perturbation in the velocity model is caused by the kinematic difference between monitor and baseline datasets. Even with large baseline velocity errors, IDWT recovers the correct magnitude and position of velocity

changes.

Another concern for time-lapse monitoring is the repeatability of surveys. In practice, shot and receiver locations are not identical between surveys, even for high-quality ocean bottom cables (Beasley et al., 1997; Yang et al., 2013). In some cases, after the initial large survey for exploration, specialized local surveys for monitoring are more economical and efficient (Hatchell et al., 2013). Deviations between survey geometries cause problems in time-lapse FWI methods that require data subtractions (Denli and Huang, 2009; Watanabe et al., 2005). In contrast, IDWT depends only weakly on the survey geometry. With a good baseline model, IDWT delivers accurate results, as long as the monitor survey illuminates an area of interest that is also well-imaged with the baseline survey. When large errors (e.g., 800 m/s) exist in the baseline model, IDWT still produces reasonable results when differences in survey geometries are considerable (e.g., 50 m).

From a computational point of view, IDWT requires two wavefield extrapolations for each migration. With the same wave equation solver, it takes twice as much time as FWI for each iteration. However, it is not necessary to simulate the full wavefield to form the images. The image warping cost function is sensitive only to misalignments, and is robust to inaccuracy in simulated waveform amplitudes. In contrast, traditional FWI needs accurate amplitudes so that differences between waveforms are reliable. We could potentially use a faster traveltime solver like ray-tracing to speed up IDWT. Another possible concern is the memory requirement for IDWT. While RTM or FWI need to store two wavefields for calculating the gradient, IDWT needs to store four wavefields, which could be too demanding in a 3D application. Symes (2007) presented an optimal checkpointing method that trades floating point operations for most of the storage in general adjoint computations. Although the memory requirement is still going to be twice that of FWI, it should be

manageable in practice.

Although the time per iteration is twice that of FWI, IDWT appears to converge more quickly. Therefore, when using IDWT before FWI to resolve velocity anomalies with high resolution, the actual computation of IDWT does not dominate the cost of the overall process. As in the first synthetic example in this study, IDWT takes only 50% of the total cpu runtime of the process. When large velocity changes exist, the cycle skipping effect makes the regular FWI cost function insensitive to velocity updates. IDWT using image warping helps to find a good starting model with correct large-scale kinematics for FWI. For initial velocity model building, ideas similar to image-warping can be implemented in the data domain to avoid cycle-skipping. However, with reflection geometries, FWI fails to invert for volumetric changes in velocity, and the result tends to be like that of a least-squares migration. Ma and Hale (2013) have successfully overcome this problem. However, to extend their method to time-lapse applications requires further study.

Beyond the theory and numerical studies presented here, we have applied IDWT to field datasets (time-lapse walkaway Vertical Seismic Profiles) that were collected from a $CO_2$ sequestration testing site, and successfully recovered P-wave velocity changes that can not be resolved by full waveform inversion (Yang et al., 2014). With very limited survey apertures and the presence of strong noise in real data, stacking images of neighboring shots would increase the signal-noise ratio and mitigate imaging artifacts without losing much angle information if the source distribution is dense. Studies with more field datasets of different acquisition conditions and different time-lapse mechanisms (e.g. water flood, gas leakage) are planned for the near future.

## CONCLUSION

We have proposed a time-lapse wavefield tomography method in the image domain for reflection data. The warping between baseline and monitor images is used as a cost function that is sensitive to smooth velocity perturbations, and robust to cycle-skipping errors. The method is accurate and wave-equation based, and requires no linearization or assumptions about the smoothness of the model. It is computationally efficient with fast convergence, and does not require the computation of angle gathers. Even with limited acquisitions, such as narrow offsets and small numbers of sources, and for complex subsurface structures, IDWT delivers reliable time-lapse inversion results. It is also robust with respect to baseline velocity errors and survey geometry discrepancies between surveys. With IDWT, kinematic effects are distinguished from other time-lapse effects, thereby providing a good foundation for subsequent analysis of amplitudes and reservoir characterization.

## ACKNOWLEDGMENTS

This work was supported by the MIT Earth Resources Laboratory Founding Members Consortium. The authors would like to especially thank Yong Ma from Conoco Philips for in-depth discussions and constructive suggestions. We also thank the associate editor, Dave Hale, Denis Kiyashchenko, and an anonymous reviewer for their insightful comments and suggestions to help improve the manuscript.

# APPENDIX A

# ADJOINT METHOD FOR IDWT

Here we present the mathematical derivation of the adjoint wavefields and the gradient for IDWT using the associate Lagrangian in the time domain. Following the approach of Plessix (2006), the steps of the derivation are: for model parameter $m$, and cost function $J(m)$,

(i) list all the state equations $F_i = 0$;

(ii) build the augmented functional $L$ by associating the independent adjoint state variables $\lambda_i$ with the state equations $F_i$;

(iii) define the adjoint-state equations by $\frac{\partial L}{\partial \lambda_i} = 0$;

(iiii) compute the gradient by $\frac{\partial L}{\partial m} = \frac{\partial J}{\partial m}$.

To make the process less complicated, we derive everything based on a single shot in a 2-D space. A more general derivation can be easily achieved by summing over all the shots. The extension to 3-D is straightforward by applying an integral over y. The least-square functional is:

$$J(m) = \frac{1}{2} \int_x \int_z |w(x,z)|^2 dxdz, \tag{A-1}$$

where $w(x,z)$ is the warping function that minimizes

$$D(w(x,z)) = \frac{1}{2} \int_x \int_z |I_1(x,z) - I_0(x, z + w(x,z))|^2 dxdz, \tag{A-2}$$

where $I_0(x,z)$ is the baseline image that stays invariant throughout the process, and $I_1(x,z)$ is the monitor image based on the slowness model $m$. The first derivative of the function with respect to $w(x,z)$ should be close to zero at the minimum point:

$$\frac{\partial D}{\partial w}(x,z) = (I_1(x,z) - I_0(x, z + w(x,z))) \frac{\partial I_0(x, z + w(x,z))}{\partial z} \approx 0. \tag{A-3}$$

$I_1(x,z)$ is obtained from the imaging condition:

$$I_1(x,z) = \int_0^T u_s(x,z,t) u_r(x,z,T-t) dt. \tag{A-4}$$

$u_s$ is the source wavefield obtained by solving the following wave equations:

$$\begin{cases} m\frac{\partial^2 u_s(t)}{\partial t^2} - \Delta u_s(t) = f_s \\ u_s(x,z,0) = 0 \\ \frac{\partial u_s(x,z,0)}{\partial t} = 0 \end{cases} . \tag{A-5}$$

$u_r$ is the receiver wavefield obtained by solving the following equations:

$$\begin{cases} m\frac{\partial^2 u_r(t)}{\partial t^2} - \Delta u_r(t) = d(T-t) \\ u_r(x,z,0) = 0 \\ \frac{\partial u_r(x,z,0)}{\partial t} = 0. \end{cases} . \tag{A-6}$$

For simplicity, the spatial boundary conditions are left unspecified because any condition that guarantees a unique solution is acceptable. In our numerical examples, we use absorbing boundary conditions.

Using the Lagrangian formulation, we associate the adjoint states $\tilde{\mu}_s^0$, $\tilde{\mu}_s^1$, $\tilde{\mu}_r^0$, $\tilde{\mu}_r^1$ with the initial conditions in Equation A-5 and A-6, respectively. Adjoint states $\tilde{\lambda}_s$ and $\tilde{\lambda}_r$ are associated with the wave equations in Equation A-5 and A-6. Adjoint states $\tilde{\phi}_I$ and $\tilde{\phi}_w$ are associated with Equation A-4 and A-3. With the operations above, the augmented functional is defined by:

$$\begin{aligned} &L(\tilde{\phi}_I, \tilde{\phi}_w, \tilde{\lambda}_s, \tilde{\lambda}_r, \tilde{\mu}_s^0, \tilde{\mu}_s^1, \tilde{\mu}_r^0, \tilde{\mu}_r^1, \tilde{u}_s, \tilde{u}_r, \tilde{I}_1, \tilde{w}, m) = \\ &\quad \int_x \int_z \frac{1}{2} |\tilde{w}(x,z)|^2 dx dz \\ &\quad - \int_0^T \langle \tilde{\lambda}_s, m\frac{\partial^2 \tilde{u}_s(t)}{\partial t^2} - \Delta \tilde{u}_s(t) - f_s \rangle_{x,z} dt - \langle \tilde{\mu}_s^0, \tilde{u}_s(0) \rangle_{x,z} - \langle \tilde{\mu}_s^1, \frac{\partial \tilde{u}_s(0)}{\partial t} \rangle_{x,z} \\ &\quad - \int_0^T \langle \tilde{\lambda}_r, m\frac{\partial^2 \tilde{u}_r(t)}{\partial t^2} - \Delta \tilde{u}_r(t) - d(T-t) \rangle_{x,z} dt - \langle \tilde{\mu}_r^0, \tilde{u}_r(0) \rangle_{x,z} - \langle \tilde{\mu}_r^1, \frac{\partial \tilde{u}_r(0)}{\partial t} \rangle_{x,z} \end{aligned}$$

$$-\langle\tilde{\phi}_I, \tilde{I}_1(x,z) - \int_0^T u_s(x,z,t)u_r(x,z,T-t)dt\rangle_{x,z}$$
$$-\langle\tilde{\phi}_w, -(\tilde{I}_1(x,z) - \tilde{I}_0(x,z+\tilde{w}(x,z))\frac{\partial\tilde{I}_0(x,z+\tilde{w}(x,z))}{\partial z}\rangle_{x,z} \quad \text{(A-7)}$$

with $\langle\tilde{\lambda}_s, \tilde{u}_s\rangle_{x,z} = \int_x\int_z \tilde{\lambda}_s(x,z)\tilde{u}_s(x,z)dxdz$ the real scalar product in space. By two integrations over $t$ by parts, we switch the second order time derivative operator from $\tilde{u}_s$ to $\tilde{\lambda}_s$:

$$\int_0^T \langle\tilde{\lambda}_s, m\frac{\partial^2\tilde{u}_s(t)}{\partial t^2}\rangle_{x,z}dt =$$
$$\int_0^T \langle m\frac{\partial^2\tilde{\lambda}_s(t)}{\partial t^2}, \tilde{u}_s\rangle_{x,z}dt + \langle\tilde{\lambda}_s(T), m\frac{\partial\tilde{u}_s(T)}{\partial t}\rangle_{x,z} - \langle\tilde{\lambda}_s(0), m\frac{\partial\tilde{u}_s(0)}{\partial t}\rangle_{x,z}$$
$$-\langle m\frac{\partial\tilde{\lambda}_s(T)}{\partial t}, \tilde{u}_s(T)\rangle_{x,z} + \langle m\frac{\partial\tilde{\lambda}_s(0)}{\partial t}, \tilde{u}_s(0)\rangle_{x,z}. \quad \text{(A-8)}$$

The same operation is applied to similar terms: $\int_0^T \langle\tilde{\lambda}_r, m\frac{\partial^2\tilde{u}_r(t)}{\partial t^2}\rangle_{x,z}dt$, $\int_0^T \langle\tilde{\lambda}_s, \Delta\tilde{u}_s(t)\rangle_{x,z}dt$ and $\int_0^T \langle\tilde{\lambda}_r, \Delta\tilde{u}_r(t)\rangle_{x,z}dt$.

With Equation A-7 and A-8, we can compute the derivatives with respect to the adjoint states, and evaluate them at $(\lambda_s, \lambda_r, u_s, u_r, \phi_I, I_1, \phi_w, w)$ to obtain the adjoint-state equations. With respect to $\tilde{u}_s$, we have equations:

$$\begin{cases} m\frac{\partial^2\lambda_s(t)}{\partial t^2} - \Delta\lambda_s(t) = \phi_I(-u_r(T-t)) \\ \lambda_s(T) = 0 \\ \frac{\partial\lambda_s(T)}{\partial t} = 0 \end{cases}. \quad \text{(A-9)}$$

With respect to $\tilde{u}_r$, we have equations:

$$\begin{cases} m\frac{\partial^2\lambda_r(t)}{\partial t^2} - \Delta\lambda_r(t) = \phi_I(-u_s(T-t)) \\ \lambda_r(T) = 0 \\ \frac{\partial\lambda_r(T)}{\partial t} = 0 \end{cases}. \quad \text{(A-10)}$$

With respect to $\tilde{I_1}$ and $\tilde{w}$ we have equations:

$$\begin{cases} -\phi_I - \phi_w(-\frac{\partial I_0(x,z+w(x,z))}{\partial z}) = 0 \\ w - \phi_w(-\Pi) = 0 \\ \Pi = (\frac{\partial I_0(z+w(x,z))}{\partial z})^2 - \frac{\partial^2 I_0(z+w(x,z))}{\partial z^2}(I_1(x,z) - I_0(x,z+w(x,z))) \end{cases} . \tag{A-11}$$

By taking the derivative of $L$ with respect to the model parameter m, we have the gradient of the cost function:

$$\frac{\partial L}{\partial m} = \frac{\partial J(m)}{\partial m} = -\int_0^T \frac{\partial^2 \lambda_s(x,z,t)}{\partial t^2} u_s(x,z,t) + \frac{\partial^2 \lambda_r(x,z,t)}{\partial t^2} u_r(x,z,t) dt \tag{A-12}$$

## REFERENCES


Arts, R., O. Eiken, A. Chadwick, P. Zweigel, B. van der Meer, and G. Kirby, 2004, Seismic monitoring at the Sleipner underground $CO_2$ storage site (North Sea): Geological Society, London, Special Publications, **233**, 181–191.

Asnaashari, A., R. Brossier, S. Garambois, F. Audebert, P. Thore, and J. Virieux, 2011, Sensitivity analysis of timelapse images obtained by differential waveform inversion with respect to reference model: SEG Technical Program Expanded Abstracts 2011.

Barkved, O. I., and T. Kristiansen, 2005, Seismic time-lapse effects and stress changes examples from a compacting reservoir: The Leading Edge, **24**, 1244–1248.

Baysal, E., D. D. Kosloff, and J. W. C. Sherwood, 1983, Reverse time migration: Geophysics, **48**, 1514–1524.

Beasley, C., R. Chambers, R. Workman, K. Craft, and L. Meister, 1997, Repeatability of 3-D ocean bottom cable seismic surveys: The Leading Edge, **16**, 1281–1286.

Bickle, M., A. Chadwick, H. Huppert, M. Hallworth, and S. Lyle, 2007, Modeling carbon dioxide accumulation at Sleipner: Implications for underground carbon storage: Earth and Planetary Science Letters, **255**, 164–176.

Biondi, B., and A. Almomin, 2012, Tomographic full waveform inversion (TFWI) by combining full waveform inversion with wave-equation migration velocity analysis: SEG Technical Program Expanded Abstracts 2012, doi:10.1190/segam2012–0275.1.

Cox, B., and P. Hatchell, 2008, Straightening out lateral shifts in time-lapse seismic: First Break, **26**.

Dadashpour, M., M. Landrø, and J. Kleppe, 2008, Nonlinear inversion for estimating reservoir parameters from time-lapse seismic data: Journal of Geophysics and Engineering, **5**, 54.

Denli, H., and L. Huang, 2009, Double-difference elastic waveform tomography in the time domain: SEG Technical Program Expanded Abstracts, **28**, 2302–2306.

Hale, D., 2013, Dynamic warping of seismic images: Geophysics, **78**, S105–S115.

Hale, D., B. Cox, and P. Hatchell, 2008, Apparent horizontal displacements in time-lapse seismic images: SEG Technical Program Expanded Abstracts 2008, 3169–3173.

Hatchell, P., K. Wang, J. Lopez, J. Stammeijer, and M. Davidson, 2013, Instantaneous 4D seismic (i4D) for offshore water injection monitoring: SEG Technical Program Expanded Abstracts 2013, 4885–4889.

Landrø, M., and J. Stammeijer, 2004, Quantitative estimation of compaction and velocity changes using 4D impedance and traveltime changes: Geophysics, **69**, 949–957.

Lumley, D. E., 2001, Time-lapse seismic reservoir monitoring: Geophysics, **66**, 50–53.

Ma, Y., and D. Hale, 2013, Wave-equation reflection traveltime inversion with dynamic warping and full-waveform inversion: Geophysics, **78**, R223–R233.

McMechan, G. A., 1983, Migration by extrapolation of time-dependent boundary values: Geophysical Prospecting, **31**, 413–420.

Plessix, R.-E., 2006, A review of the adjoint-state method for computing the gradient of a functional with geophysical applications: Geophysical Journal International, **167**, 495–503.

Shragge, J., T. Yang, and P. Sava, 2013, Time-lapse image-domain tomography using adjoint-state methods: Geophysics, **78**, A29–A33.

Sun, D., and W. W. Symes, 2012, Waveform inversion via nonlinear differential semblance optimization: SEG Technical Program Expanded Abstracts 2012, doi:10.1190/segam2012–1190.1.

Symes, W. W., 2007, Reverse time migration with optimal checkpointing: Geophysics, **72**,

SM213–SM221.

Tarantola, A., 1984, Inversion of seismic reflection data in the acoustic approximation: Geophysics, **49**, 1259–1266.

Versteeg, R., 1994, The Marmousi experience: Velocity model determination on a synthetic complex data set: The Leading Edge, **13**, 927–936.

Virieux, J., and S. Operto, 2009, An overview of full-waveform inversion in exploration geophysics: Geophysics, **74**, WCC1–WCC26.

Watanabe, T., S. Shimizu, E. Asakawa, and T. Matsuoka, 2005, Differential waveform tomography for time-lapse crosswell seismic data with application to gas hydrate production monitoring: SEG Technical Program Expanded Abstracts 2005.

Yang, D., M. Fehler, A. Malcolm, and L. Huang, 2011, Carbon sequestration monitoring with acoustic double-difference waveform inversion: A case study on SACROC walkaway VSP data: SEG Technical Program Expanded Abstracts, **30**, 4273–4277.

Yang, D., M. Fehler, A. Malcolm, F. Liu, and S. Morton, 2013, Double-difference waveform inversion of 4D ocean bottom cable data: Application to Valhall, North Sea: SEG Technical Program Expanded Abstracts 2013, 4966–4970.

Yang, D., A. Malcolm, M. Fehler, and L. Huang, 2014, Time-lapse walkaway vertical seismic profile monitoring for CO2 injection at the SACROC enhanced oil recovery field: A case study: Geophysics, **79**, B51–B61.

Yang, D., Y. Zheng, M. Fehler, and A. Malcolm, 2012, Target-oriented time-lapse waveform inversion using virtual survey: SEG Technical Program Expanded Abstracts 2012, doi:10.1190/segam2012–1308.1.

## LIST OF FIGURES

1 (a).The three-layer density model for both baseline and monitor surveys. Red Stars denote the locations of the shots, and blue triangles denote the receiver locations. (b). Differences in the P-wave velocities between baseline and monitor surveys. Maximum velocity change is 800m/s. (c) The baseline image $I_0$ obtained using one shot gather and the constant velocity model. (d) The monitor image $I_1$ obtained using one shot gather and the constant velocity model. The center part of the second reflector is vertically shifted due to the absence of the velocity anomaly in (b).

2 The image warping function $w(x, z)$ calculated from Figure 1(c) and 1(d). Units on the color scale are image points. Positive values indicate upwards shifts. The maximum warping is 4 grid points (i.e. 40 meters).

3 (a). The velocity changes found by IDWT with 5 sources. The anomaly is correctly positioned. However, the limited aperture of the acquisition makes the waves travel primarily in the vertical direction, so the recovered velocity anomaly is smeared vertically. (b). The monitor migration image obtained using one shot gather and the velocity model inverted by IDWT. The second reflector is correctly positioned. (c). The velocity changes refined by FWI after IDWT. The amplitude differences and subtle phase shifts between data and simulation are minimized to resolve the fine details in the velocity model. FWI has significantly reduced the vertical smearing observed in Figure 3(a). (d). The velocity changes obtained with standard FWI applied to the monitor data, starting from the baseline constant background velocity model. The Gaussian anomaly is barely visible. An artificial reflector is erroneously created to account for data differences. This failure is due to the combined effects of cycle skipping and limited survey geometry.

4 Cost function curves for IDWT, FWI after IDWT, and FWI only. The cost func-

tions are normalized by their values before the 1st iterations. IDWT converged within 10 iterations. FWI after IDWT converged much slower. The cost function of FWI starting from the constant velocity plateaued after 10 iterations.

5 (a). The six-layer baseline and time-lapse density model. Layers in the center are smaller in thickness than the size of time-lapse velocity anomaly (white circle). (b), (c) and (d) show the IDWT results with 1 shot, 10 shots and 20 shots, respectively. As we include more shots, the amplitude distribution within the anomaly is corrected. The vertical smearing is well constrained by the reflector. The maximum velocity change is closer to the true value as the changes are confined to a smaller area.

6 (a). True baseline velocity model with a Gaussian anomaly with peak velocity change of 200 m/s. We assume the anomaly is not known, and use a constant velocity model for the baseline migrations. (b). True time-lapse velocity changes with peak value of 200 m/s. (c). True time-lapse velocity model I with two Gaussian anomalies ((a) plus (b)). (d). The time-lapse velocity changes found using IDWT.(e). True time-lapse velocity model II. We increase the peak amplitude of the Gaussian anomaly in the baseline velocity model to 800 m/s, and use the same time-lapse velocity changes as in (b). (f). The time-lapse velocity changes inverted by IDWT. The shape of the anomaly is distorted because of the large error in the baseline velocity model, but the basic location and amplitude is preserved.

7 This figure shows robustness tests of IDWT to random source positioning errors and baseline velocity errors. The sources in the monitor survey are randomly shifted $\pm 10$ meters from their baseline positions. The baseline velocity error for each case has maximum value of 0 (a), 200 (b) and 800 m/s (c). Compared to the case where there is no mispositioning in Figures 5(d), 6(d), and 6(f), the random source positioning error has little effect on the performance of IDWT.

8 Robustness tests of IDWT against source positioning error plus baseline velocity error. In the 3x3 plot, the monitor survey sources are systematically shifted 10, 20 and 50 meters from their correct positions for each column, respectively. The baseline velocity error for each row has maximum value of 0, 200 and 800 m/s. Black dotted circles mark the areas where false velocity changes are resolved due to the baseline velocity error, which is at the same location as shown in Figure 6(e).

9 Migrated images for one baseline shot and one shifted monitor shot. Dotted lines show the wave paths along which velocities are updated. Portions of the monitor migrated image marked as unconstrained image (dashed circles), have no corresponding image points from the baseline image.

10 (a). The center part of the original Marmousi model is used as the true baseline velocity model. The maximum source-receiver offset is 2 km. Five shots (red stars) are used to generated synthetic data. (b). True time-lapse velocity model with a negative velocity change marked with a black dashed line. The black arrow points to the area where the boundary of the changes is located in the middle of the layer. We designed this half-layer velocity change intentionally to show how IDWT would smear the changes within a layer.

11 (a). A smoothed version of the Marmousi model is used as the baseline model for migration. (b). Migrated image for one shot (red star). Areas pointed to by arrows are poorly imaged due to the limited receiver aperture. Dashed lines mark the boundary of the velocity changes. The interfaces above and below the anomaly are well-imaged.

12 (a). The true time-lapse velocity changes. The anomaly is smooth at its boundary (dashed lines). (b). The inverted time-lapse changes using IDWT with 5 shots. The black arrow points to the area where the inverted velocity changes diffuse across the boundary of the true changes (dashed lines), and are both smeared towards and bounded by the lower

interface of this layer.

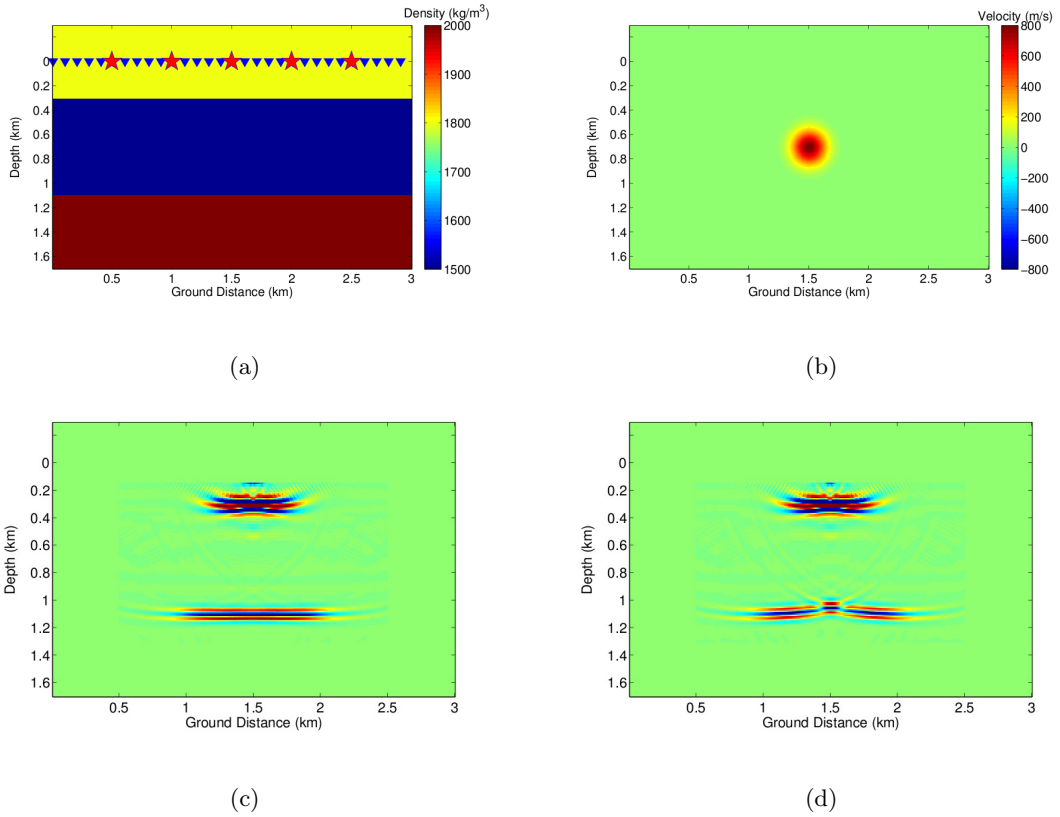


Figure 1: (a).The three-layer density model for both baseline and monitor surveys. Red Stars denote the locations of the shots, and blue triangles denote the receiver locations. (b). Differences in the P-wave velocities between baseline and monitor surveys. Maximum velocity change is 800m/s. (c) The baseline image $I_0$ obtained using one shot gather and the constant velocity model. (d) The monitor image $I_1$ obtained using one shot gather and the constant velocity model. The center part of the second reflector is vertically shifted due to the absence of the velocity anomaly in (b).

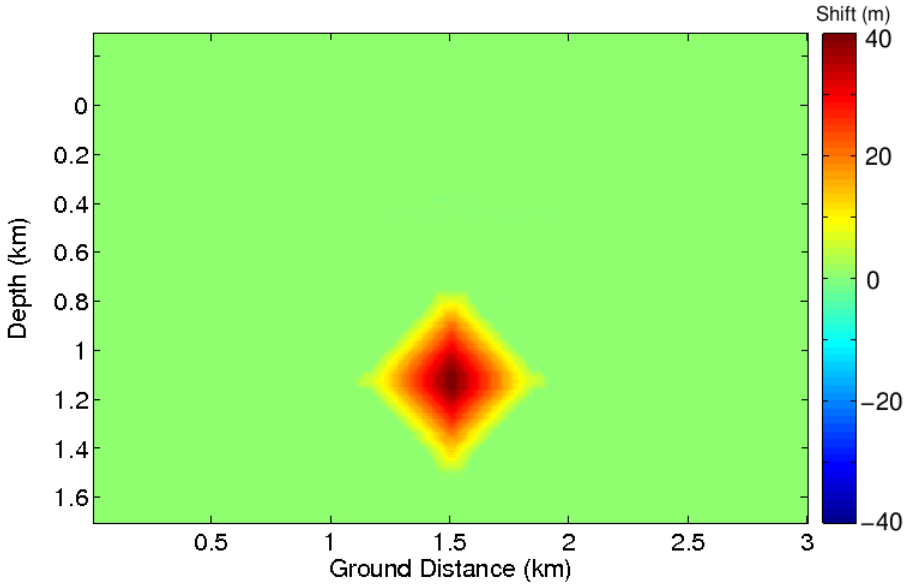


Figure 2: The image warping function $w(x, z)$ calculated from Figure 1(c) and 1(d). Units on the color scale are image points. Positive values indicate upwards shifts. The maximum warping is 4 grid points (i.e. 40 meters).

– **GEO-2013-0424**

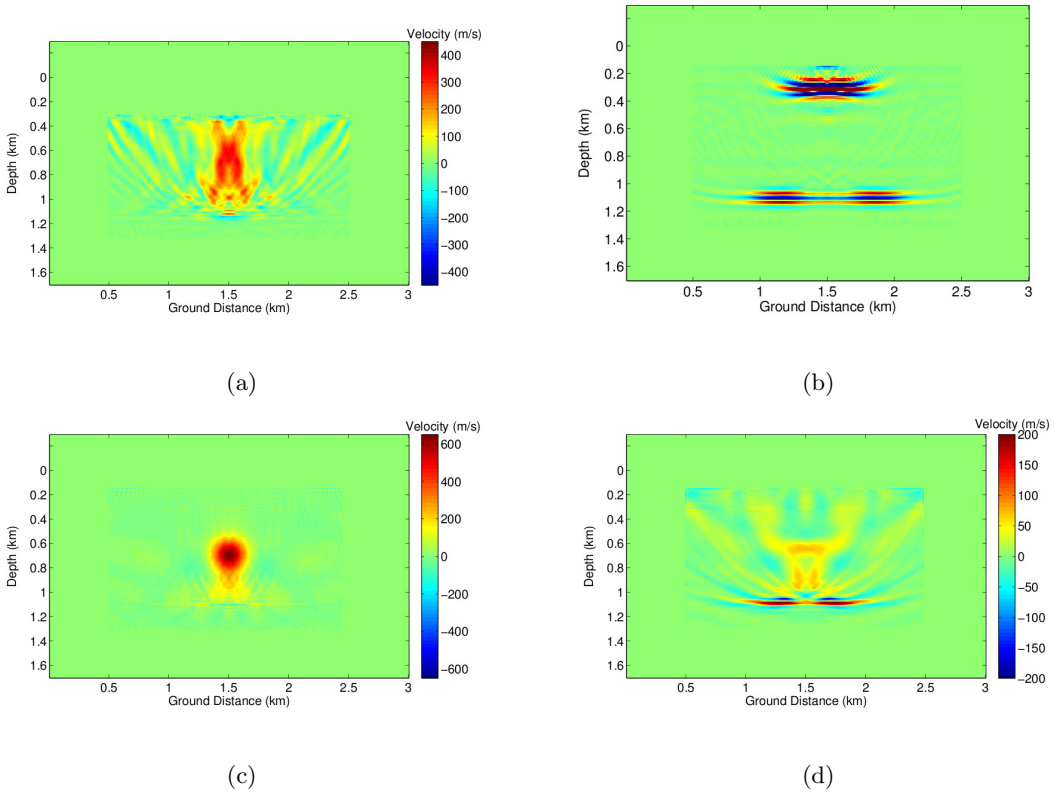


Figure 3: (a). The velocity changes found by IDWT with 5 sources. The anomaly is correctly positioned. However, the limited aperture of the acquisition makes the waves travel primarily in the vertical direction, so the recovered velocity anomaly is smeared vertically. (b). The monitor migration image obtained using one shot gather and the velocity model inverted by IDWT. The second reflector is correctly positioned. (c). The velocity changes refined by FWI after IDWT. The amplitude differences and subtle phase shifts between data and simulation are minimized to resolve the fine details in the velocity model. FWI has significantly reduced the vertical smearing observed in Figure 3(a). (d). The velocity changes obtained with standard FWI applied to the monitor data, starting from the baseline constant background velocity model. The Gaussian anomaly is barely visible. An artificial reflector is erroneously created to account for data differences. This failure is due to the combined effects of cycle skipping and limited survey geometry.

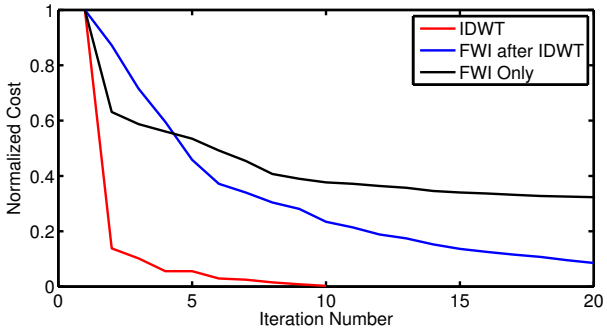


Figure 4: Cost function curves for IDWT, FWI after IDWT, and FWI only. The cost functions are normalized by their values before the 1st iterations. IDWT converged within 10 iterations. FWI after IDWT converged much slower. The cost function of FWI starting from the constant velocity plateaued after 10 iterations.

– **GEO-2013-0424**

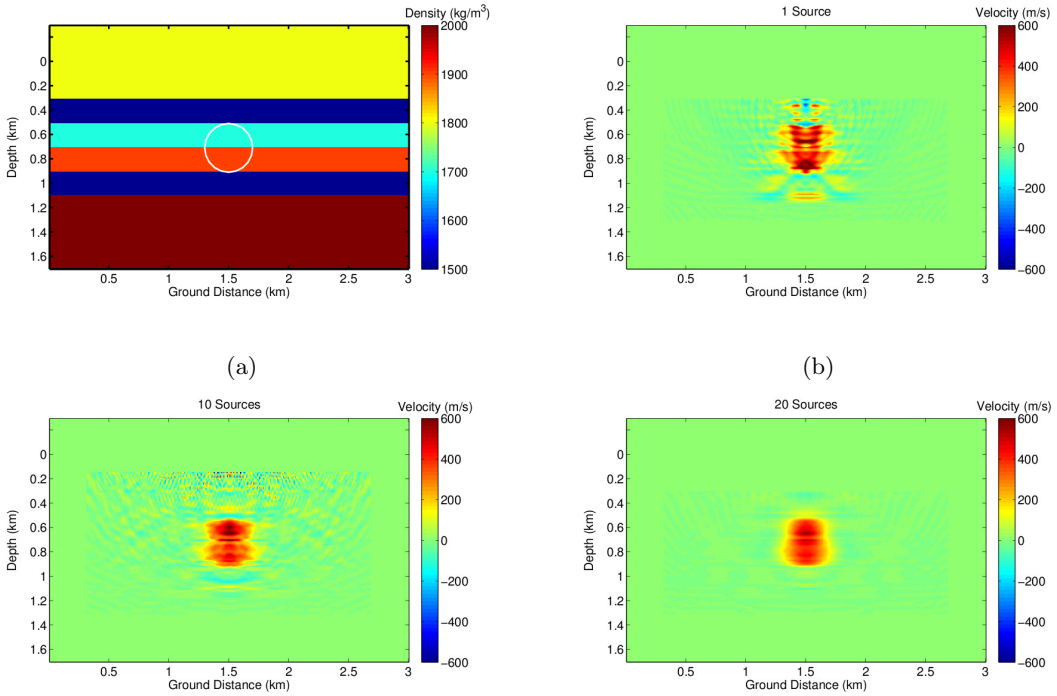


Figure 5: (a). The six-layer baseline and time-lapse density model. Layers in the center are smaller in thickness than the size of time-lapse velocity anomaly (white circle). (b), (c) and (d) show the IDWT results with 1 shot, 10 shots and 20 shots, respectively. As we include more shots, the amplitude distribution within the anomaly is corrected. The vertical smearing is well constrained by the reflector. The maximum velocity change is closer to the true value as the changes are confined to a smaller area.

– **GEO-2013-0424**

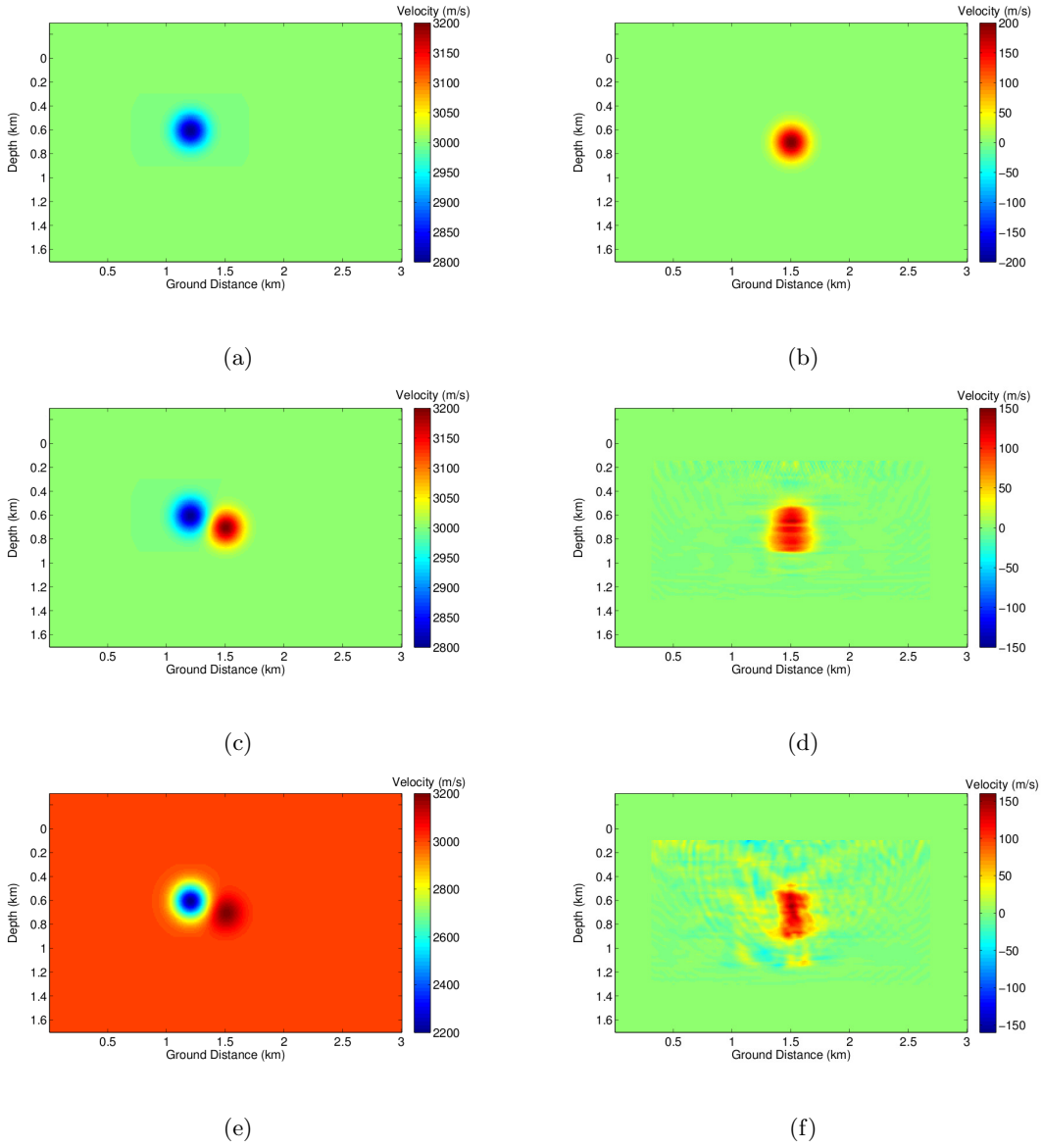


Figure 6: (a). True baseline velocity model with a Gaussian anomaly with peak velocity change of 200 m/s. We assume the anomaly is not known, and use a constant velocity model for the baseline migrations. (b). True time-lapse velocity changes with peak value of 200 m/s. (c). True time-lapse velocity model I with two Gaussian anomalies ((a) plus (b)). (d). The time-lapse velocity changes found using IDWT.(e). True time-lapse velocity model II. We increase the peak amplitude of the Gaussian anomaly in the baseline velocity model to 800 m/s, and use the same time-lapse velocity changes as in (b). (f). The time-lapse velocity changes inverted by IDWT. The shape of the anomaly is distorted because of the

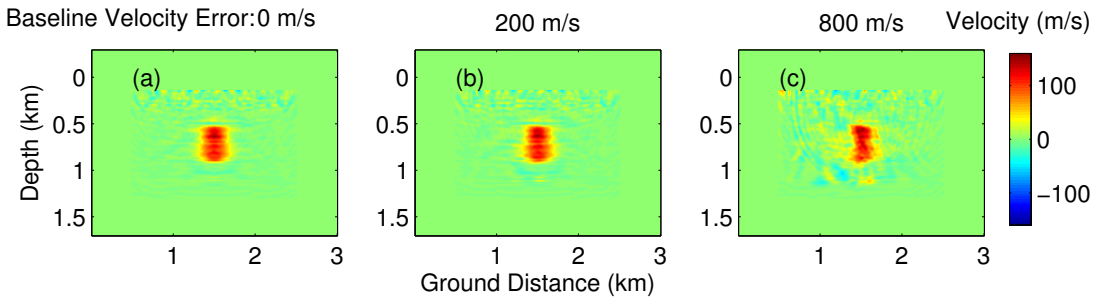


Figure 7: This figure shows robustness tests of IDWT to random source positioning errors and baseline velocity errors. The sources in the monitor survey are randomly shifted ±10 meters from their baseline positions. The baseline velocity error for each case has maximum value of 0 (a), 200 (b) and 800 m/s (c). Compared to the case where there is no mispositioning in Figures 5(d), 6(d), and 6(f), the random source positioning error has little effect on the performance of IDWT.

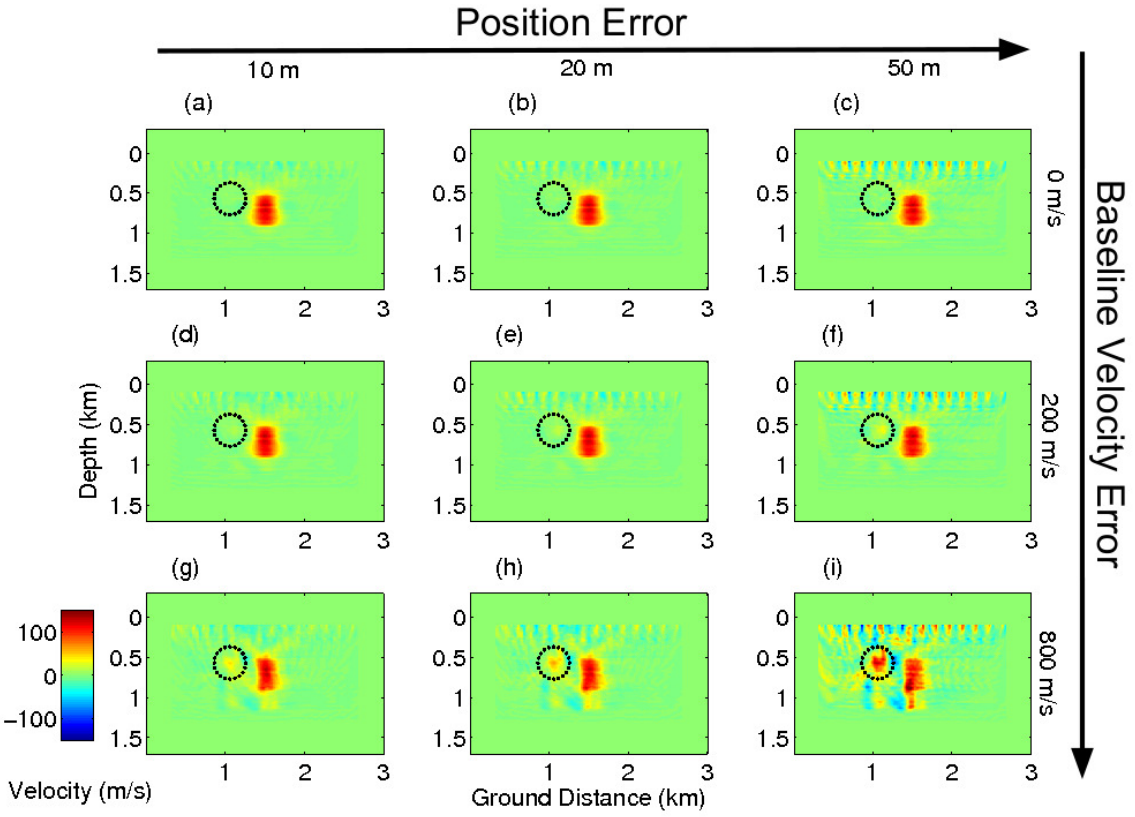


Figure 8: Robustness tests of IDWT against source positioning error plus baseline velocity error. In the 3x3 plot, the monitor survey sources are systematically shifted 10, 20 and 50 meters from their correct positions for each column, respectively. The baseline velocity error for each row has maximum value of 0, 200 and 800 m/s. Black dotted circles mark the areas where false velocity changes are resolved due to the baseline velocity error, which is at the same location as shown in Figure 6(e).

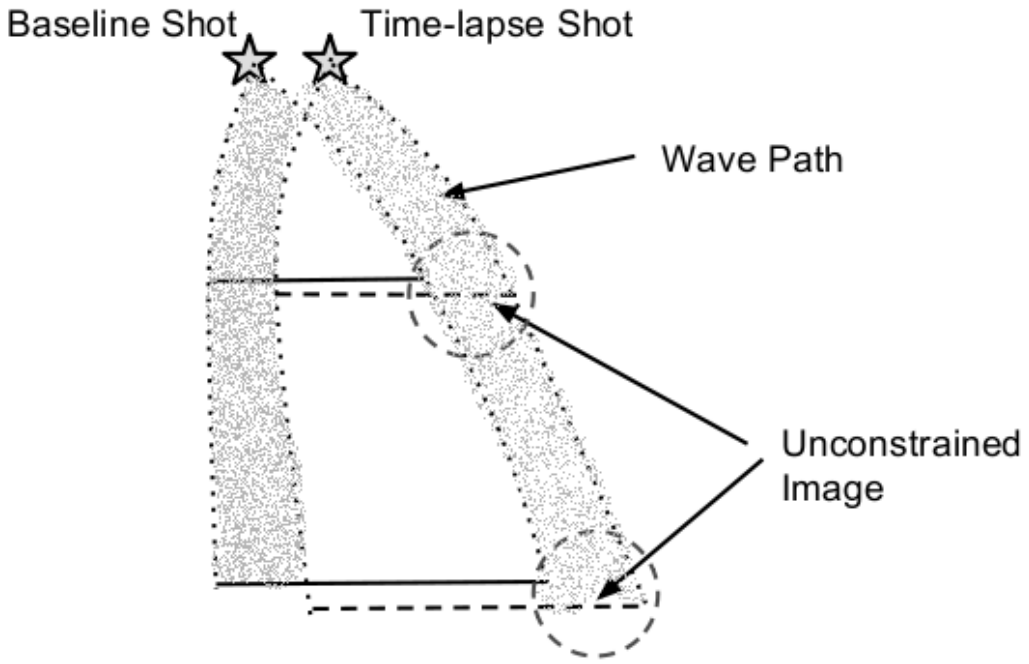


Figure 9: Migrated images for one baseline shot and one shifted monitor shot. Dotted lines show the wave paths along which velocities are updated. Portions of the monitor migrated image marked as unconstrained image (dashed circles), have no corresponding image points from the baseline image.

– **GEO-2013-0424**

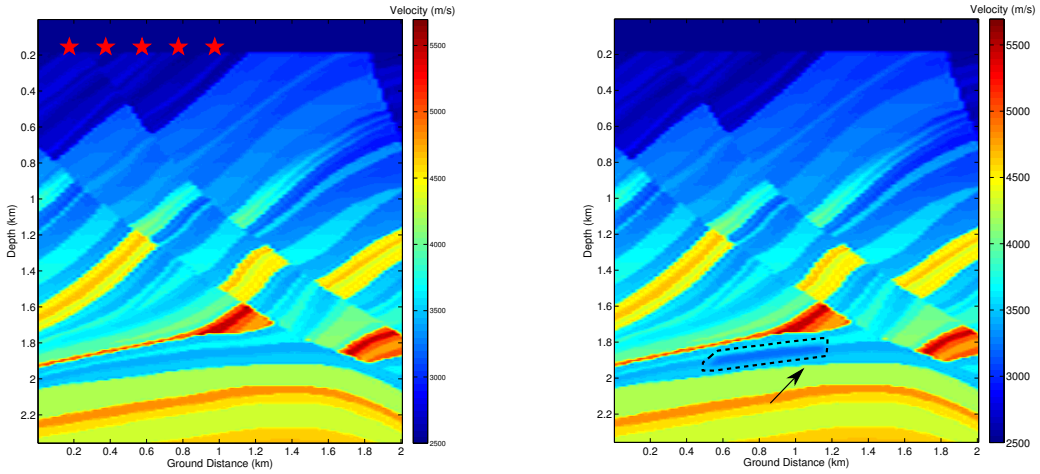


(a) (b)

Figure 10: (a). The center part of the original Marmousi model is used as the true baseline velocity model. The maximum source-receiver offset is 2 km. Five shots (red stars) are used to generated synthetic data. (b). True time-lapse velocity model with a negative velocity change marked with a black dashed line. The black arrow points to the area where the boundary of the changes is located in the middle of the layer. We designed this half-layer velocity change intentionally to show how IDWT would smear the changes within a layer.

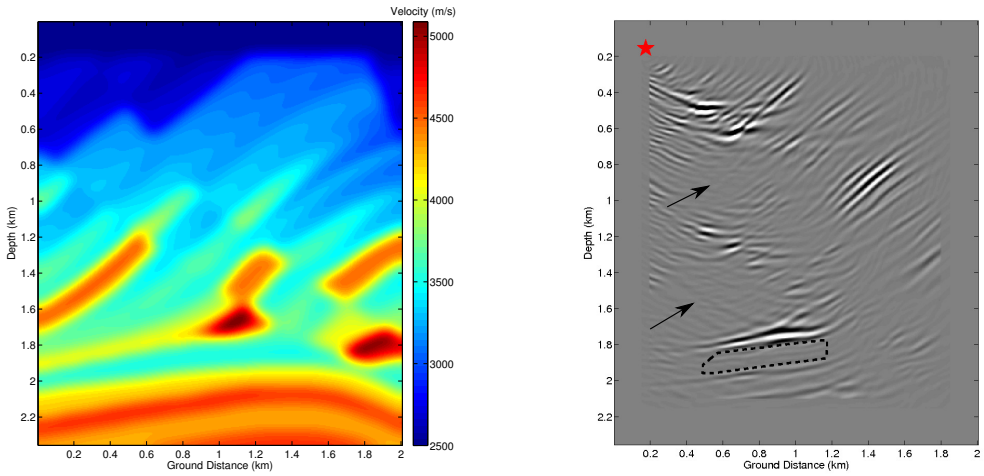


(a) (b)

Figure 11: (a). A smoothed version of the Marmousi model is used as the baseline model for migration. (b). Migrated image for one shot (red star). Areas pointed to by arrows are poorly imaged due to the limited receiver aperture. Dashed lines mark the boundary of the velocity changes. The interfaces above and below the anomaly are well-imaged.

– **GEO-2013-0424**

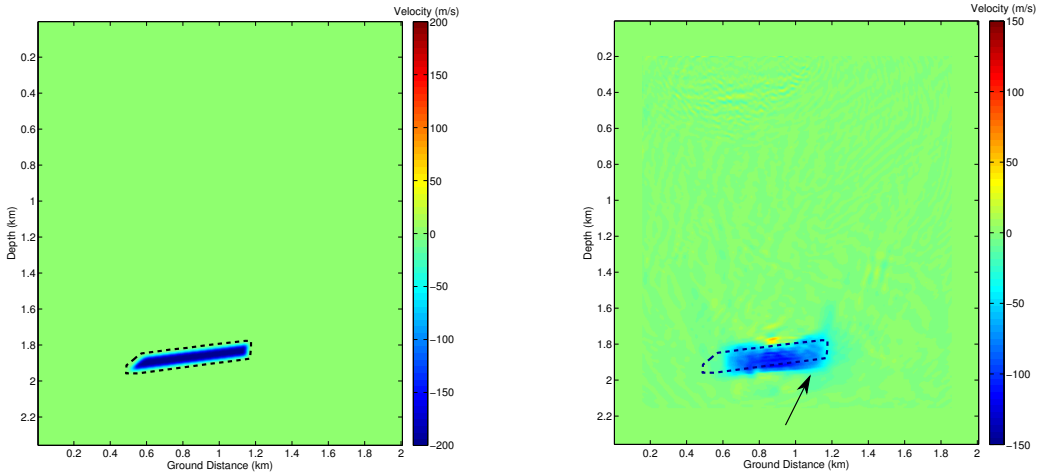


(a) (b)

Figure 12: (a). The true time-lapse velocity changes. The anomaly is smooth at its boundary (dashed lines). (b). The inverted time-lapse changes using IDWT with 5 shots. The black arrow points to the area where the inverted velocity changes diffuse across the boundary of the true changes (dashed lines), and are both smeared towards and bounded by the lower interface of this layer.

– **GEO-2013-0424**